A Finite Difference informed Random Walker (FDiRW) solver for strongly inhomogeneous diffusion problems

Zirui Mao[1*], Yulan Li[1], Robert Montgomery[1], Agnes Grandjean[3], Hans-Conrad zur Loye[2], Shenyang Hu[1*]

[1] Pacific Northwest National Laboratory, Richland, WA 99352,
[2] Department of Chemistry and Biochemistry, University of South Carolina, Columbia, SC 29208, USA
[3] CEA, DES, ISEC, DMRC, Uni Montpellier, Marcoule, France

E-mail: zirui.mao@pnnl.gov; shenyang.hu@pnnl.gov

Abstract

In nature, many complex multi-physics coupling problems exhibit strong diffusivity inhomogeneity. For instance, in the context of radionuclide absorption by porous wasteform materials within a flowing waste stream, the difference of species' diffusivity in solid and liquid phases spans by 3~8 orders of magnitude. To solve the diffusion equations with strongly inhomogeneous diffusivity, traditional discretization-based methods, such as the Finite Difference Method (FDM), require infinitesimally small-time steps ($<10^{-10}$) as high spatial resolutions are employed in most microstructure evolution processes, leading to prohibitively high computational costs. This work developed an integrated numerical approach (FDiRW: Finite Difference informed Random Walk) to tackle this challenge. The idea is that utilizing the Random Walk concept, the fast diffusion is modelled as a superposition of point source's solution for a concentration distribution while FDM is used to obtain the point source's solution at each node. A mesh-coarsening algorithm is developed to generate an exclusive coarse mesh for FDiRW approach to maximize its efficiency. The effectiveness of the coarse mesh-based FDiRW approach is validated by benchmarking Finite Difference solutions. Numerical results demonstrated that FDiRW achieves a remarkable 1000x computational efficiency improvement over FDM while preserving desired accuracy for a medium-sized model of $192 \times 192 \times 192$ grids. As models scale up, a floating-point operations (PLOPs) analysis of the FDiRW algorithm reveals that its computational complexity grows quadratically in terms of the number of nodes employed in computation.

Keywords: Finite Difference Method, Finite Difference informed Random Walker, strongly inhomogeneous diffusivity, radionuclide ion exchange, porous wasteform materials.

1. Introduction

Complex multi-physics coupling problems in nature often involve phenomena spanning a broad range of time scales. For instance, in nuclear materials, the long-term radiation decay of fuel materials coexists with the rapid evolution of radiation-induced defects across polycrystalline structures. Similarly, during nuclear waste stream treatment, the slow diffusion of radionuclides within porous wasteform materials occurs alongside the very fast diffusion and advection in liquids. Experimental investigations of such systems are challenging due to the extreme time scales involved, either too long or too short for direct

observation and analysis. Numerical simulations complement experimental studies by providing insights into the system behavior under varying conditions and enabling the exploration of phenomena at scales inaccessible to experiments.

However, the multi-physics and multi-scale nature of these systems present significant computational challenges. In particular, strongly inhomogeneous diffusivity observed in many natural systems necessitates the use of extremely small-time steps (denoted as Δt) in numerical simulations. This requirement stems from the need to accurately capture rapid diffusive processes occurring within small regions characterized by the grid size of Δh. The time marching step Δt must be chosen sufficiently small such that the rapid diffusion around a certain node does not extend beyond the nearest layer of nodes, which yields the stability criterion $\Delta t \leq F_s \frac{\Delta h^2}{D_{max} \times 2 \times N_d}$ [1], where F_s is a safety factor less than 1 to ensure the stability and accuracy of numerical methods, D_{max} is the largest diffusivity, and N_d is the spatial dimensionality of the problem solved numerically. Consequently, when the diffusivity spans a wide range, say 8 orders of magnitude, the smallest diffusivity implies a long diffusion duration, while the largest diffusivity governs the time step Δt required in numerical simulations. In such cases, the numerical model may need to be iterated as many as 10^{11} times or more, resulting in prohibitively high computational demands. This high computational load is rooted in the discretization concept employed by most mature numerical methods, such as the Finite Element Method (FEM) [2, 3] and the Finite Difference Method (FDM) [4-6].

Although there exist many adaptive mesh techniques [7, 8] to alleviate the computational burden by allowing for coarser grids in regions far from the solid-liquid interface, fine meshing is still required on/near the interface to capture critical concentration gradients accurately. This requirement of local fine mesh causes small time steps and heavy computational burdens, particularly when the liquid phase exhibits significantly fast diffusion. Moreover, our study focusses primarily on the fast diffusion near the interface, while simplifying the minor effects of fast diffusion in the far-field region, that is suitable to coarse mesh, by assuming instant uniform concentration based on conservation principles. This configuration makes traditional adaptive mesh techniques less effective for close-field diffusion studies.

To address these computationally challenging in material with strongly inhomogeneous diffusivity, this study proposes a more efficient and accurate numerical solver. Instead of adopting the discretization concept used in traditional numerical methods, we employ the superposition concept for handling fast diffusion, inspired by the Random Walk model applied to predict isotropic diffusion within an infinitely large domain [9-11]. The Random Walk model traditionally assumes isotropic diffusion, where particles spread evenly across an infinite domain, with the diffusion across domain being treated as the sum of such individual behaviors. For instance, the Random Walker model has been successfully applied to dendritic growth studies [12]. However, this assumption doesn't hold in complex porous systems with non-isotropic diffusion and boundary effects, and the diffusion distances from one location to another is not always determinant. Therefore, instead of applying the standard Random Walk expression, the Finite Difference Method is used to calculate the long-time diffusion of a point source at each node in the domain, termed the Finite Difference integrated Random Walk (FDiRW) solver. The FDiRW has two apparent advantages over FDM in computing fast diffusion. First, it significantly reduces the small-time step limitation. Second, it dramatically alleviates the small spatial size requirement, as the density distribution after a long-time fast diffusion within the whole domain becomes relatively smooth, negating the need for fine mesh resolution. Thus, the FDiRW holds promising potential for computational efficiency compared to the discretization-based FDM.

This study takes the radionuclide uptake in porous nuclear wasteform materials as a model system to showcase the performance potential of the FDiRW solver in terms of accuracy and efficiency for handling computationally challenging from strongly inhomogeneous diffusivity.

2. Integrated model of radionuclide absorption in porous nuclear wasteform materials

In the treatment of nuclear waste streams, porous wasteform particles ranging in size from 1 to 500 microns are immersed in a nuclear waste solution containing radionuclide ions [13-15]. These ions diffuse through the solution and are absorbed at the surface of the wasteform particles, after which their movement within the solid phase is significantly slower—typically by factors of 3 to 8 orders of magnitude compared to their diffusion in the liquid phase [16, 17]. To accurately simulate the kinetics of radionuclide absorption, numerical models are essential in elucidating the absorption mechanism and optimizing the design of effective wasteform materials and treatment processes.

Given the prohibitive computational demands for simulating such large-scale systems, two key simplifications are employed. First, the ratio of waste stream volume to the wasteform particle volume is analyzed. Simulating a single wasteform particle, surrounded by its corresponding waste stream volume, provides a suitable approximation of the radionuclide absorption kinetics without sacrificing the accuracy of the physical processes involved. Second, the computational domain is divided into near-field and far-field regions, whose boundary is defined by a spherical surface, as illustrated by the dashed circle in Figure 1. The near-field, which includes the pores of the wasteform particle, represents the region of rapid diffusion. That is, only the near-field is computationally analyzed, while the far-field treated as having a instantly uniform radionuclide concentration. This simplification significantly reduces the computational load by focusing on the most critical region for absorption kinetics while still capturing the broader system behavior.

Thus, the computational procedure consists of four primary steps: (1) fast diffusion of radionuclide ions in the near-field liquid, (2) absorption of ions at the particle surface, (3) slow diffusion within the solid wasteform particle, and (4) determination of the radionuclide concentration in the far-field based on mass conservation. This multi-physics process is modelled using a phase field approach, which has been successfully validated in our earlier studies. [18]:

$$\frac{\partial c_m(\boldsymbol{r},t)}{\partial t} = \nabla \cdot \left(D_m \nabla \left(\frac{\mu_m}{RT} \right) \right) + \dot{R}_m, \qquad m = \text{S in } solid \text{ and } m = \text{L in } liquid\ phase, \tag{1}$$

where $\boldsymbol{r} = (x, y, z)$ represents the spatial coordinate, and t denotes time. c_m is the instantaneous concentration of radionuclide ions in phase m, while D_m is the inhomogeneous diffusivity of radionuclide ions in phase m. The term $\dot{R}_m$ represents the absorption rate at the solid/liquid interface. R and T stand for the gas constant and temperature in K, respectively. μ_m is the chemical potential governing the diffusion behavior in the liquid phase and the absorption capacity of the solid phase.

The first term on the right-hand side of Eq. (1) describes ion diffusion, which is governed by the gradient of chemical potential, driving the concentration c_i towards its equilibrium value c_m^{eq}. The second term accounts for the absorption of radionuclide ions at the solid/liquid interface.

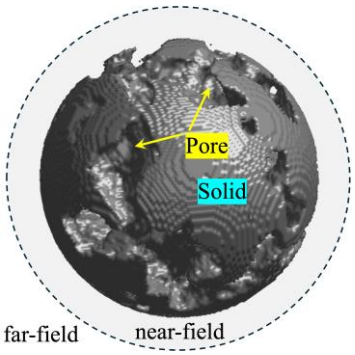

Figure 1 Computational domains surrounding the porous wasteform particle. The porous wastform particle is generated numerically with phase field modelling by referring to the microstructure information measured in experiment.

Fast diffusion in near-field liquid. Fast diffusion within the near-field liquid phase is characterized by a diffusivity, D_L, which is significantly greater than that in the solid phase, D_S. In this study, we assume that $D_L = 1000D_S$, reflecting the real scenario where diffusion in the liquid phase is typically several orders of magnitude faster than that in the solid. The fast diffusion occurring in the near-field liquid phase is driven by the gradient of chemical potential, μ_L, within the liquid phase, expressed as:

$$\mu_L = \mu_L(\boldsymbol{r}, t) = A_L\big(c_L(\boldsymbol{r}, t) - c_L^{eq}\big). \tag{2}$$

Here, c_L^{eq} is the equilibrium concentration in the liquid phase, indicating the remaining concentration of radionuclides in the liquid phase after the solid particle reaches its absorption capacity, as measured experimentally. The free surface coefficient A_L is associated with the second derivative of the chemical free energy with respect to concentration c_L at the equilibrium concentration c_L^{eq} [19, 20]. These parameters are tailored to the properties of the liquid phase and are essential for modelling the rapid diffusion of radionuclide ions near the wasteform particles. The initial concentration of radionuclide ions exist in the liquid phase is denoted as c_L^0, and the total initial concentration in the solutioin is calculated as: $Q_L^0 = c_L^0 N_L$, with N_L being the total number of liquid nodes in the whole liquid phase.

Slow diffusion in solid. The slow diffusion occurring in the solid phase is mathematically represented similarly to the fast diffusion in the near-field liquid phase. Specifically, the thermodynamic properties that determine the absorption capacity of the wasteform particles are described by the chemical potential μ_S, which is expressed as:

$$\mu_S = \mu_S(\boldsymbol{r}, t) = A_S\big(c_S(\boldsymbol{r}, t) - c_S^{eq}\big). \tag{3}$$

Here, c_S^{eq} represents the equilibrium concentration in the solid phase, indicating the maximum concentration of radionuclides absorbed by the solid particle as measured through experimental measurements. The absorption capacity of wasteform particles is thus defined as $Q_S^e = c_S^{eq} N_S$, with N_S being the total number of solid nodes. A_S is the free energy coefficient for the solid phase.

Radionuclide absorption at solid/liquid interface. In simulating the radionuclide absorption by the solid surface, a one-layer sharp interface between solid and liquid node is employed, as illustrated in Figure 2.The nodes from each phase that are directly

connected to nodes in the other phase are considered interface nodes. Only these interface nodes consider the interface reaction term in Eq. (1), which represents the radionuclide absorption. Generally, the interface reaction occurs only when the concentration in the liquid exceeds its equilibrium value, *i.e.*, $c_L(t) > c_L^{eq}$, meanwhile the concentration in the solid is below its equilibrium value, *i.e.*, $c_S(t) < c_S^{eq}$. To account for this, we use the modified Pseudo-Second-Order reaction rate

$$\dot{R} = k f_L f_S \tag{4}$$

with the parameters f_L and f_S being

$$f_L = \begin{cases} 0, & as\ c_L(t) \le c_L^{eq} \\ \frac{c_L(t) - c_L^{eq}}{c_L^{eq}}, & as\ c_L(t) > c_L^{eq} \end{cases} \tag{5}$$

$$f_S = \begin{cases} \frac{c_S^{eq} - c_S(t)}{c_S^{eq}}, & as\ c_S(t) < c_S^{eq} \\ 0, & as\ c_S(t) \ge c_S^{eq} \end{cases}, \tag{6}$$

where k is the reaction rate coefficient. For interface nodes in the solid phase, the reaction rate is $\dot{R}_S = \dot{R}$, while for the interface nodes in liquid phase, their interface rate is $\dot{R}_L = -\dot{R}$. Our previous study has demonstrated the effectiveness of this interface reaction formulation in modeling radionuclides absorption problems [18].

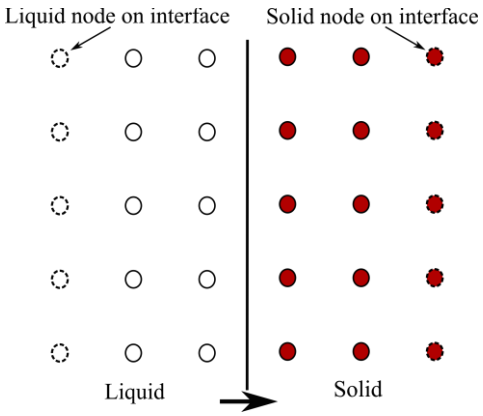

Figure 2 Illustration of the sharp interface employed in simulations.

Concentration uniformization in far-field liquid. With the assumption of instant uniformness of radionuclide concentration within far-field liquid and the concentration conservation constraint, the concentration $c_L^{far-field}$ at far-field liquid is updated at every time step with

$$c_L^{far-field}(t) = \frac{\Sigma c_{S+L}(t_0) - \Sigma c_L^{near-field}(t) - \Sigma c_S(t)}{V_L^{far-field}} \tag{7}$$

Here, $\Sigma c_{S+L}(t_0)$ is the total concentration of radionuclides in the whole domain including the solid phase and liquid phase (including both near-field and far-field) initially. $\Sigma c_L^{near-field}(t)$ and $\Sigma c_S(t)$ are the instant total concentration in the near-field liquid and solid, respectively. $V_L^{far-field}$ is the volume of far-field liquid. Obviously, the averaged uniform concentration $c_L^{far-field}$ conserves the concentration in the whole domain explicitly.

When solving the differential form in Eq. (1), the Laplacian term $\nabla^2 F$ at spatial point (i, j, k) is approximated with the 3-D central Finite Difference scheme:

$$\nabla^2 F_{i,j,k} = \frac{F_{i+1,j,k}+F_{i-1,j,k}+F_{i,j+1,k}+F_{i,j-1,k}+F_{i,j,k+1}+F_{i,j,k-1}-6F_{i,j,k}}{\Delta h^2} \tag{8}$$

while the temporal derivative is approximated straightforwardly with the forward Eulerian scheme:

$$c(t+\Delta t) = c(t) + \frac{\partial c(\mathbf{r},t)}{\partial t}\Delta t \tag{9}$$

where the critical time step Δt is determined with the criterion:

$$\Delta t = 0.2 \times \frac{\Delta h^2}{6D_L}. \tag{10}$$

Consider a particle with a radius r_P. In implementation, the liquid phase within a sphere of radius $r_P + 5\Delta h$ is defined as the near-field liquid phase. Numerical experiments have quantified the distribution of computational time across the four key processes involved in modeling radionuclide absorption kinetics in porous wasteform particles. For a particle with $r_P = 50\Delta h$, results reveal a significant imbalance: the fast diffusion process in the near-field liquid consumes a staggering 99.82% of the total computational time. In contrast, the other processes require only a small fraction of resources, with slow diffusion in the solid phase accounting for 0.13%, concentration uniformization in the far-field liquid contributing 0.04%, and interface reactions at the solid/liquid interface taking just 0.01%. While the primary goal of this study is to understand the radionuclide absorption kinetics of porous wasteform particles, the fast diffusion process in the near-field liquid is crucial for investigating the effects of microstructural features—such as porosity, contact area, and particle size—on absorption kinetics. These features significantly influence diffusion behavior and, consequently, the absorption of radionuclides. Despite the importance of fast diffusion in the near-field liquid, dedicating 99.82% of computational resources to this process is disproportionately high, especially when compared to the computational demands of the other processes. This imbalance highlights the need for more efficient strategies to reduce the computational load associated with solving the fast diffusion process, bringing it closer to the computational effort required by the other physical processes.

All relevant parameters and material properties are summarized in Table 1. The initial and equilibrium concentrations in both the solid and liquid phases are configured to maintain concentration conservation between the initial and equilibrium states, in accordance with the volume fractions of the liquid and solid phases and experimental data [21].

Table 1 Parameter values and material properties employed in simulation.

Δh	10×10^{-9} $[m]$	$\frac{A_L}{RT}$	2×10^3
Δt	500 $[\mu s]$	c_S^{eq}	1.0
Δt_{fd}	0.5 $[\mu s]$	c_L^{eq}	1.0×10^{-5}
D_S	1.0×10^{-17} $[m^2/s]$	c_S^0	1.0×10^{-6}
D_L	1.0×10^{-14} $[m^2/s]$	c_L^0	2.12×10^{-3}
$\frac{A_S}{RT}$	2×10^3	k	0.05 $[1/s\ ]$
when $r_P = 50\Delta h$			
V_{Solid}	3.667×10^{-13} [mL]	V_{Liquid}	1.834×10^{-10} [mL]
$V_L^{far-field}$	1.830×10^{-10} [mL]	$\Sigma c_{S+L}(t_0) = V_{Liquid} c_L^0$ where c_L^0 is normalized	3.888×10^{-13} [mL]

3. FDiRW solver for fast diffusion in the near-field liquid

3.1 FDiRW algorithm

This FDiRW approach, allowing for significantly larger time steps for solving fast diffusion phenomena, has shown success in addressing strongly inhomogeneous diffusivity of species across polycrystalline structures with thin grain boundaries [22, 23]. It conceptualizes the diffusion process in the liquid phase as a superposition of each liquid node's isolated diffusion event, inspired by the Random Walker model [9-11].

In other word, for a liquid node i at location $\mathbf{r}_i$ with a concentration $c_i(t, \mathbf{r}_i)$ at time t, once knowing the proportion p_{ji} of concentration diffused from each other liquid node, labeled as j, with initial concentration $c_j(t, \mathbf{r}_j)$ at time t, we can calculate the updated concentration after a period of diffusion, say Δt, with:

$$c(t + \Delta t, \mathbf{r}_i) = \sum_{j=1}^{N_L} p_{ij}(\Delta t) c_j(t, \mathbf{r}_j) + p_i^{BC}(\Delta t) c_{far-field}(t) \tag{11}$$

Here, Δt is the duration of fast diffusion, which can be much larger than the time step Δt used in Finite Difference solver when solving the fast diffusion process.

$p_{ij}(\Delta t)$ is the solution of diffusion at node $\mathbf{r}_i$ at time (Δt) for a point source at node $\mathbf{r}_j$. $p_{ij}(\Delta t)$, which is kind of the Green's function [24] for a point source with isotropic diffusivity in an infinite medium, is a solution with diffusion only along the connected pores. Therefore, for our case studies, there is no analytic solution for a point source because the diffusion takes place along the connected pores inside the particle. Similarly, $p_i^{BC}(\Delta t)$ is a solution at time (Δt) along the connected pores inside the particle for a constant concentration $c_{far-field} = 1$ on the boundary. So $p_{ij}(\Delta t)$ and $p_i^{BC}(\Delta t)$ are two fundamental solutions which only depend on diffusivity, pore structure, geometries of particle and boundary as well as the node $\mathbf{r}_j$ and $\mathbf{r}_i$. Once we have the solutions $p_{ij}(\Delta t)$ and $p_i^{BC}(\Delta t)$ for given simulation domain including the geometry of particle, pore structure inside the particle, and simulation cell (boundaries), the solution at $t + \Delta t$ for given concentration $c_j(t, \mathbf{r}_j)$ at time

(t) and node $\mathbf{r}_j$ can be calculated by Eq. (11). With a fixed diffusion time Δt and a constant diffusivity, the solutions $p_{ij}(\Delta t)$ and $p_i^{BC}(\Delta t)$ are constant and therefore can be precalculated only one time for given the simulation domain.

For our case studies, where diffusion is rapid along the connected pores inside the particle, no Green's function is available for comparison. However, we did compare the p-matrix to the analytical Green's functions in 1-D, 2-D, and 3-D cases under constant and isotropic diffusivity in an infinite domain. The analytical solutions, known as Green's functions for 1-D, 2-D, and 3-D diffusion [24], are

$$p_{ij}(r_{ij},\Delta t)=\frac{1}{\sqrt{4\pi D\Delta t}}\exp\left(-\frac{r_{ij}^2}{4D\Delta t}\right) \text{ in one dimension} \tag{12}$$

$$p_{ij}(r_{ij},\Delta t)=\frac{1}{4\pi D\Delta t}\exp\left(-\frac{r_{ij}^2}{4D\Delta t}\right) \text{ in two dimension} \tag{13}$$

$$p_{ij}(r_{ij},\Delta t)=\frac{1}{(4\pi D\Delta t)^{\frac{3}{2}}}\exp\left(-\frac{r_{ij}^2}{4D\Delta t}\right) \text{ in three dimension} \tag{14}$$

where D is the diffusivity, r_{ij} is the distance of two nodes i and j. From these equations, it is clear that a constant D and a fixed Δt yield a constant p_{ij} as r_{ij} is also constant. The $\mathbf{p}$ matrix obtained from Finite Different method is the same to the analytical solution from numerical aspects. This has been well-verified by our previous paper [22].

In matrix format, the FDiRW approach represented by Eq. (11) can be represented as

$$\mathbf{c}(t+\Delta t)=\mathbf{p}(\Delta t)\mathbf{c}(t)+\mathbf{p}_{BC}(\Delta t)c_{far-field}(t) \tag{15}$$

with

$$\mathbf{c}=\begin{bmatrix}c_1\\c_2\\\vdots\\c_{N_L}\end{bmatrix},\mathbf{p}=\begin{bmatrix}p_{11}&p_{12}&\cdots&p_{1N_L}\\p_{21}&p_{22}&\cdots&p_{2N_L}\\\vdots&\vdots&\ddots&\vdots\\p_{N_L1}&p_{N_L2}&\cdots&p_{N_LN_L}\end{bmatrix},\mathbf{p}_{BC}=\begin{bmatrix}p_1^{BC}\\p_2^{BC}\\\vdots\\p_{N_L}^{BC}\end{bmatrix} \tag{16}$$

Within a fixed time-step Δt, the concentration proportion p_{ij} diffused from one liquid node, j, to another, i, remains constant. This makes $\mathbf{p}$ and $\mathbf{p}_{BC}$ in Eq. (12) preconditioned coefficient matrix and vector, not requiring update during computation. Once the coefficient matrix $\mathbf{p}$ and vector $\mathbf{p}_{BC}$ are determined, the concentration field in the liquid phase after a time period of Δt can be updated straightforwardly with Eq. (12).

Since the elements in the n-th column of $\mathbf{p}$ matrix represent the distribution of concentration proportions of the node n across the whole near-field liquid domain after diffusion, it can thus be determined by solving the diffusion equation (or the phase-field equation for liquid phase) associated with an initial condition of

$$c(t_0)=\begin{cases}1, & at\ node\ n\\0, & at\ the\ nodes\ other\ than\ node\ n\end{cases} \tag{17}$$

and a no-flux boundary condition at the interface between near-field and both far-field and solid phase. Following this rule, all the columns in $\mathbf{p}$ can be determined numerically. Note that the calculated diffusion period of fast diffusion is Δt, which is

the time step of slow diffusion in solid phase. Also, the time step employed when solving the fast diffusion with the Finite Difference scheme, Δt_{fd}, is much smaller than Δt as shown in Table 1.

For the boundary condition, the related coefficient vector, $\mathbf{p}_{\mathrm{BC}}$, corresponds to the contribution from the far-field liquid that is assumed uniform in space and constant in time ($c = 1$ is assumed) during the fast diffusion process of near-field liquid. Thus, its elements can be obtained by solving the corresponding diffusion or phase-field equation associated with an initial condition of $c(t_0) = 0$ inside the near-field/far-field interface. For boundary condition (BC), the liquid/solid interface is still assigned a no-flux BC, while the near-field/far-field interface is assigned a Dirichlet boundary condition $c \equiv 1$.

Since the FDiRW approach does not take the discretization concept in spatial and temporal, the diffusion interval Δt can extend for a considerable duration as long as the diffusion process in the liquid phase within that timeframe can be viewed as a pseudo-isolated system. Here, the "pseudo-isolated" indicates that the liquid phase experiences minimal interaction with external systems (that is the solid particle's surface in this study) or that external systems can be considered steady, *i.e.*, maintaining constant concentration. Basically, for this particular problem, it is proper to assume a constant concentration for the external system during the time step of slow diffusion in the solid phase, during which time interval the total concentration in solid is assumed constant when solving the slow diffusion in solid with the explicit Finite Difference Method. In other word, the FDiRW solver employs an identical time step as the slow diffusion process, which is 10^3 times larger than the time step required by the explicit Finite Difference method, promising significant efficiency gains.

3.2 Coarse mesh-based FDiRW

While the FDiRW solver offers efficiency benefits with larger time steps, its main limitation lies in substantial data storage requirements for large-scale problems. Specifically, the coefficient matrix **p,** with dimensions $N_L \times N_L$ (where N_L is the total number of liquid nodes), demands significant storage as N_L is large. For instance, in a medium-sized 3D model of dimensions $200 \times 200 \times 200$, assuming 50% of nodes are liquid, N_L would be 4×10^6. Consequently, **p** would have 16×10^{12} elements, requiring approximately 100 terabytes of memory storage, exceeding the capacity of most existing HPC machines.

To address this issue, we employ a coarse mesh in the FDiRW approach. A smooth concentration distribution resulting from long-time fast diffusion makes fine mesh unnecessary. Liquid nodes are grouped spatially, with each group containing multiple nodes. The node closest to the group's center is chosen as the representative liquid node. Only these representative nodes are considered in FDiRW computation, reducing the coefficient matrix's dimensions to $N_{rl} \times N_{rl}$, where the total number of representative nodes N_{rl} can be much smaller than N_L, thus improving memory efficiency and computational speed.

Note that although only representative nodes are used in FDiRW computation, the fine mesh (or full liquid nodes) is employed when calculating elements in the coefficient matrix **P** to achieve better accuracy. The capital letters such as **P**, C, I, J are used to distinguish them at the representative nodes from those at the regular nodes. Specifically, we determine the proportion of concentration moving to each representative node from others by solving the diffusion equation with an initial condition:

$$c(t_0) = \begin{cases} 1, & at\ representative\ node\ I. \\ 0, & at\ the\ nodes\ other\ than\ node\ I \end{cases} \tag{18}$$

using the explicit finite difference method based on fine mesh.

After obtaining the concentration at each liquid node, the proportion of concentration moving from representative node I to representative node J is calculated using:

$$P_{JI}(\Delta t) = \frac{\sum_{j=1}^{N_J} c_j(t_0+\Delta t)(\Delta h)^d}{\sum_{j=1}^{N_J}(\Delta h)^d} \tag{19}$$

where c_j is the concentration at liquid node j within group J, N_J is the total number of liquid nodes in group J, Δh is grid size for uniform grid, and d is the dimensionality of the problem. The elements of the boundary condition-related vector $\mathbf{P}_{BC}$ are calculated similarly. Since the product of concentration and grid size represents mass, the transformation in Eq. (19) rigid follows mass conservation.

To use the coarse mesh-based FDiRW solver, the dimension of the concentration matrix must be consistent with the coefficient matrix **P**. Thus, the concentration distribution in the fine mesh needs to be mapped to the coarse mesh before FDiRW computation. After each FDiRW iteration, the concentration in the coarse mesh is remapped back to the fine mesh for interface reaction calculation.

The mapping process from fine mesh to coarse mesh is akin to Eq. (19):

$$C(t, \mathbf{r}_I) = \frac{\sum_{i=1}^{N_I} c(t,\mathbf{r}_i)(\Delta h)^d}{\sum_{i=1}^{N_I}(\Delta h)^d} \tag{20}$$

While the re-mapping process from coarse mesh to fine mesh is done with

$$c(t + \Delta t, \mathbf{r}_i) = C(t + \Delta t, \mathbf{r}_I) \tag{21}$$

That derives from the assumption that all liquid nodes within the same group have the same concentration. These mapping and re-mapping treatments are simple and have been proven sufficiently accurate and align with mass conservation. To distinguish the concentration vector **c** with full liquid nodes (*i.e.*, fine mesh), the concentration vector with representative nodes (*i.e.*, coarse mesh) is denoted as **C**. Similarly, c and C are used to distinguish the concentration in fine and coarse meshes, respectively. The procedure of performing FDiRW computation based on coarse mesh is presented in Figure 3.

Typically, the fewer representative liquid nodes selected in FDiRW computation, the more efficient the solver becomes. However, using too few representative nodes may compromise accuracy. To achieve a balance between efficiency and accuracy, we conducted numerical experiments and chose a coarse grid where a representative node corresponds to an average of 125 actual liquid nodes, providing a balanced approach.

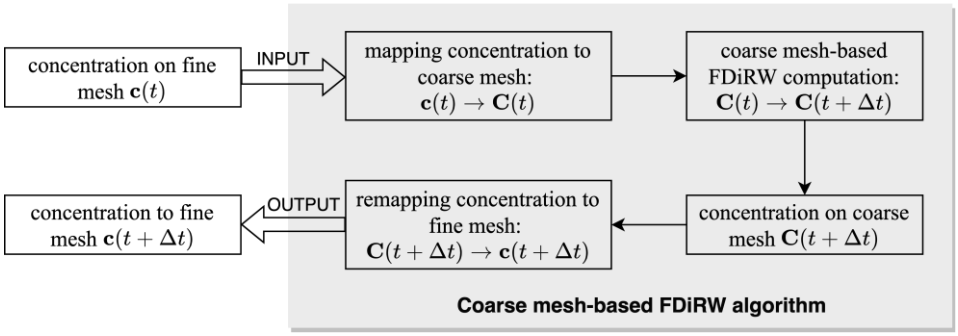

Figure 3 Flowchart of coarse mesh-based FDiRW algorithm for solving fast diffusion in near-field liquid domain.

3.3 Mesh-coarsening algorithm

Selecting appropriate liquid nodes to represent the coarse mesh in the FDiRW solver is challenging due to the irregular distribution of liquid nodes in the porous structure. Existing adaptive meshing algorithms [7, 8], which typically rely on spatial-oriented coarsening that groups close nodes together, are unsuitable for this study. Because spatially close nodes may have long diffusion paths between them, such as the liquid nodes A and B in Figure 4, where they are completed separated by the intermediate solid nodes. In such scenarios, assigning them to a same coarse grid would be impractical.

To address this, we identify suitable representative liquid nodes by solving the diffusion equation associated with a single point source $c = 1$ at a randomly chosen liquid node using the explicit Finite Difference Method. After a diffusion period of Δt, liquid nodes with concentrations above a threshold value c_{th} are grouped together as they likely have close diffusion distances. These grouped liquid nodes are used to determine the representative liquid node closest to the group's center. The liquid nodes in this group are then assigned to that representative node. This process is repeatedly applied to the remaining ungrouped liquid nodes until all liquid nodes have been assigned to corresponding representative nodes.

The resolution of the coarse mesh is controlled by the threshold value c_{th}, with larger c_{th} resulting in coarser meshes. In this study, we choose $c_{th} = 0.04$ to achieve a balance between accuracy and efficiency.

However, the random selection of liquid nodes as single point source during the mesh-coarsening process introduces uncertainty in classifying liquid nodes into groups, leading to variations in group sizes. This often results in numerous small groups, increasing the dimension of the coefficient matrix **P** without significant accuracy benefits but reducing efficiency. To mitigate this issue, a further group-merging treatment is applied to small groups with fewer than 20 nodes. Another round of simulation is conducted with a single point source $C = 1$ at these 'small' representative nodes. The 'small' representative node is then assigned to the group whose representative node has the largest concentration after diffusion (suggesting shortest diffusion distance from the 'small' representative node). However, if the total concentration of all other representative nodes is smaller than that of the interested small representative node, indicating the small group is isolated, it will not be merged with other groups. The detailed procedure of mesh-coarsening algorithm is presented in Figure 5.

The numerical tests shown in Figure 6 indicate the significant reduction in the number of small groups by taking the group-merging treatment. This reduction in small groups leads to a substantial decrease in the total number of groups, N_{rl}, from 11,033

to 2,515. Consequently, the dimension of the coefficient matrix **P** is reduced to $2{,}515 \times 2{,}515$, requiring only approximately 50 megabytes of memory storage.

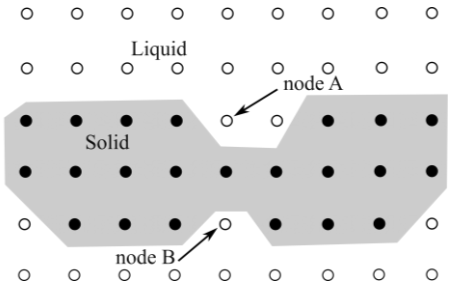

Figure 4 Illustration of two spatially close liquid nodes A and B having long diffusion path. They should be assigned to two different groups despite close distance between them.

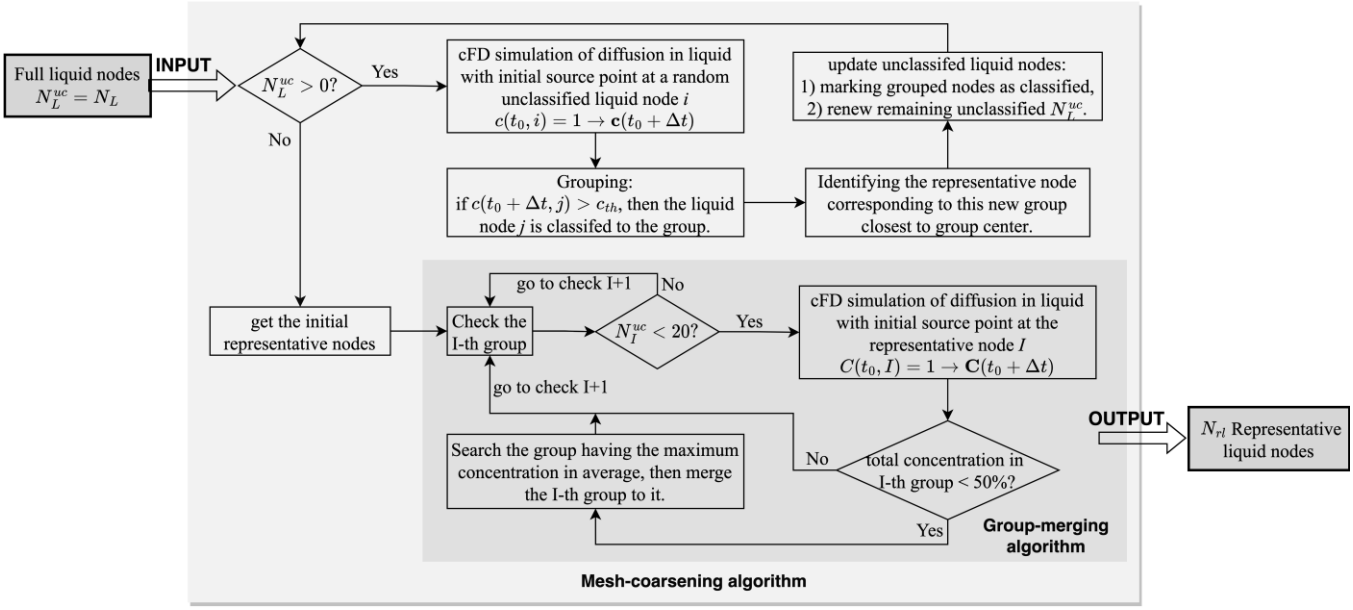

Figure 5 Flowchart of mesh-coarsening algorithm to identify representative liquid nodes. N_L^{uc} is the total number of remaining liquid nodes that are not classified to a group.

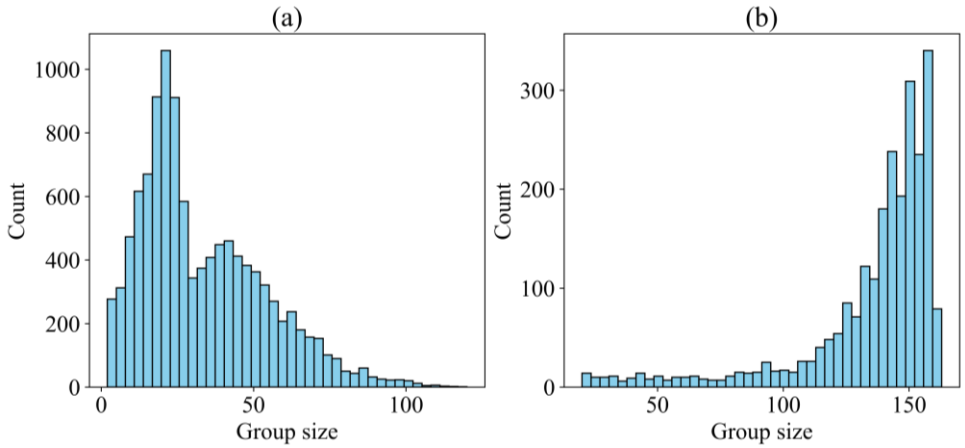

Figure 6 Distribution of group sizes before (a) and after (b) taking the group-merging treatment.

3.4 Flowchart

The overall flowchart of the proposed integrated solver for solving the strongly inhomogeneous diffusion problem across a porous wasteform particle is presented in Figure 7.

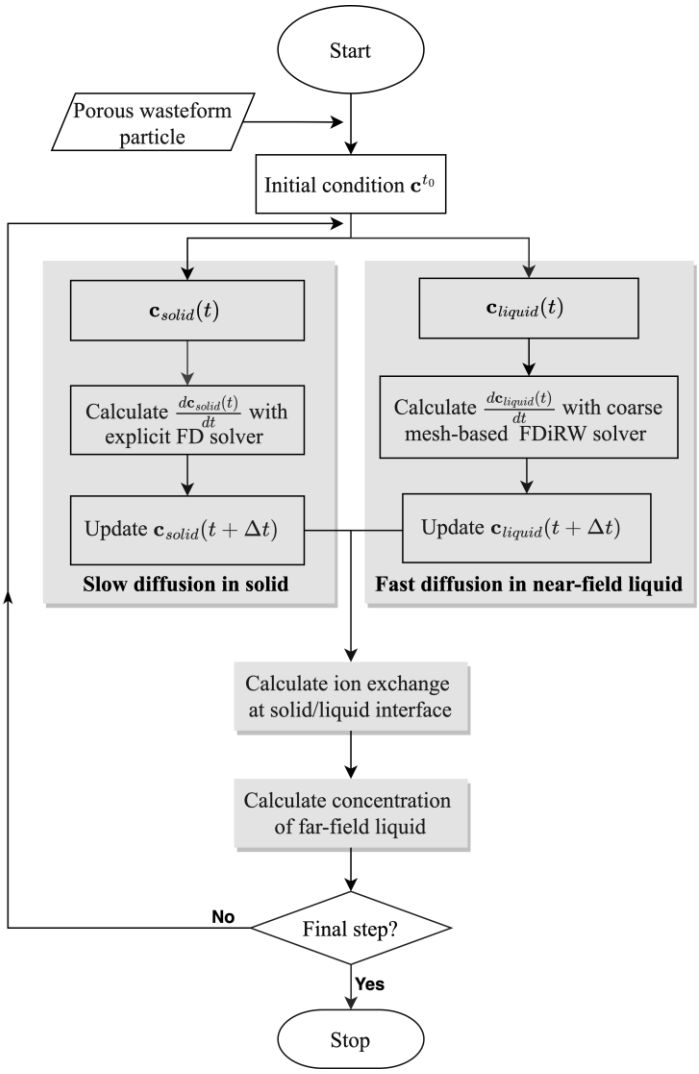

Figure 7 Flowchart of integrated solver for solving the strongly inhomogeneous diffusion problem across a porous wasteform particle.

4. Verification and Applications

The effectiveness of the proposed coarse mesh-based FDiRW solver is evaluated by comparing it to the benchmarking explicit Finite Difference method when solving the fast diffusion process in the near-field liquid. Two integrated numerical frameworks are compared: FD-FD, where both solid and liquid diffusion are solved with the explicit Finite Difference method, and FD-FDiRW, where the FDiRW solver is used for liquid diffusion instead.

Figure 8 displays concentration contours in the near-field liquid and solid phases on a selected cross-section obtained from both numerical frameworks. While the FDiRW solver produces a concentration contour in the liquid (Figure 8 (b)) appearing less smooth due to coarse mesh usage compared to FD (Figure 8 (a)), it accurately reproduces the concentration gradient in the near-field liquid, with higher concentrations near the particle surface and lower concentrations in the core area of the porous particle. Notably, the coarse mesh-based FDiRW solver has negligible impact on the resultant solid phase contours

(Figure 8 (c) and (d)), indicating the minimal influence on radionuclide absorption kinetic. Due to the higher concentration maintained in the near-field liquid close to the particle surface, radionuclides are primarily absorbed at the solid particle's surface interface, while the particle's core region retains minimal concentration level in the initial stage.

To further assess the influence of the proposed solver on radionuclide absorption kinetics, we monitor the total concentration of radionuclides that are absorbed by the wasteform particle and that remaining in the liquid phase. The numerical results presented in Figure 9 reveal that the kinetic curves obtained from FDiRW match precisely with those from the benchmarking FD-FD, affirming the desirable accuracy performance of the coarse mesh-based FDiRW solver for solving fast diffusion in the liquid phase.

In Figure 10, we compare the computational efficiency between FD-FD and FD-FDiRW. The computation involves four main components: interface reaction, slow diffusion in the solid phase, fast diffusion in the near-field liquid close to the solid particle, and update of concentration in the far-field liquid based on concentration conservation, as listed in Figure 7. It is observed that when using the Finite Difference Method to solve fast diffusion in the liquid, it consumes approximately 99.8% of the total computational time, as shown in Figure 10 (a). However, this proportion significantly reduces to a desirable level of 34.0% when using the coarse mesh-based FDiRW solver, as shown in Figure 10 (b). The total CPU run times for FD-FD and FD-FDiRW are 91,099.4 sec and 241.4 sec, respectively, as seen in Figure 10 (c). Specifically, the fast diffusion part consumes 90,940 sec in FD-FD, and only 82 sec in FD-FDiRW, as shown in Figure 10 (d). This demonstrates FDiRW's efficiency advantage, being 1000x faster than Finite Difference for fast diffusion in near-field liquid thanks to its utilization of larger time steps and coarse mesh, leading to an overall 400x enhancement of the entire framework.

In summary, the proposed coarse mesh-based FDiRW solver offers a desirable computational tool for handling fast diffusion in the liquid phase with an affordable computation demand.

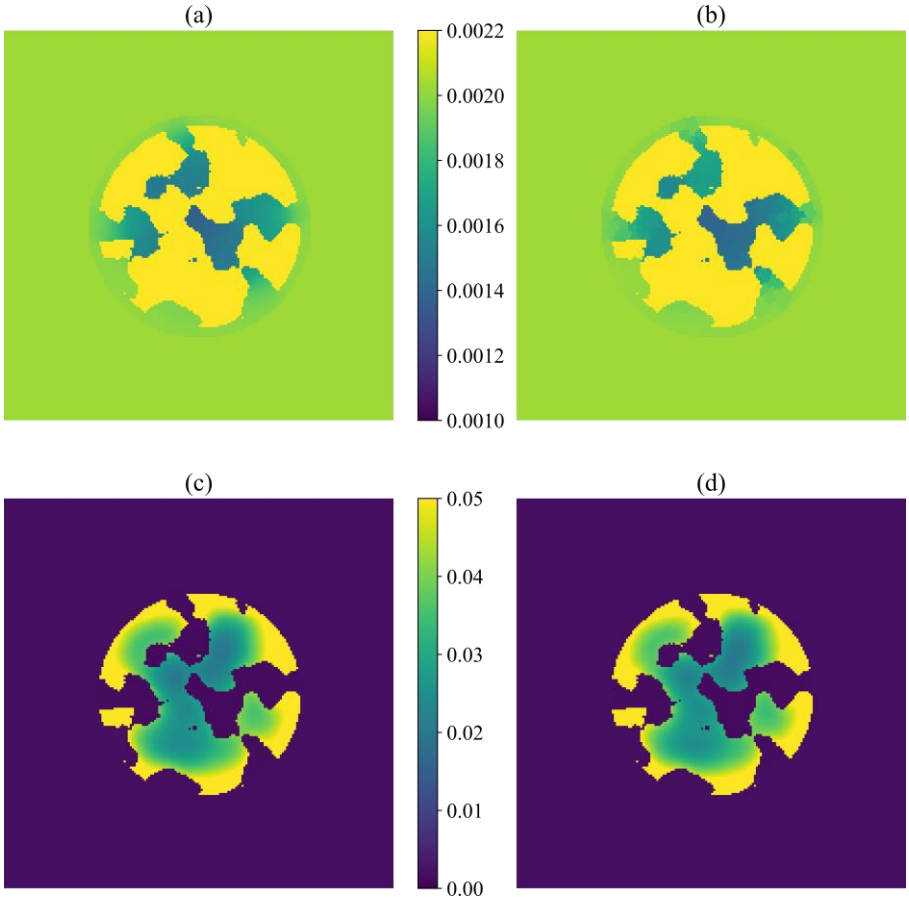

Figure 8 Screenshots of concentration fields obtained from simulations at $t = 0.5\ sec$. (a) Concentration in near-field liquid from FD-FD; (b) Concentration in near-field liquid from FD-FDiRW; (c) Concentration in solid phase from FD-FD; (d) Concentration in solid phase from FD-FDiRW.

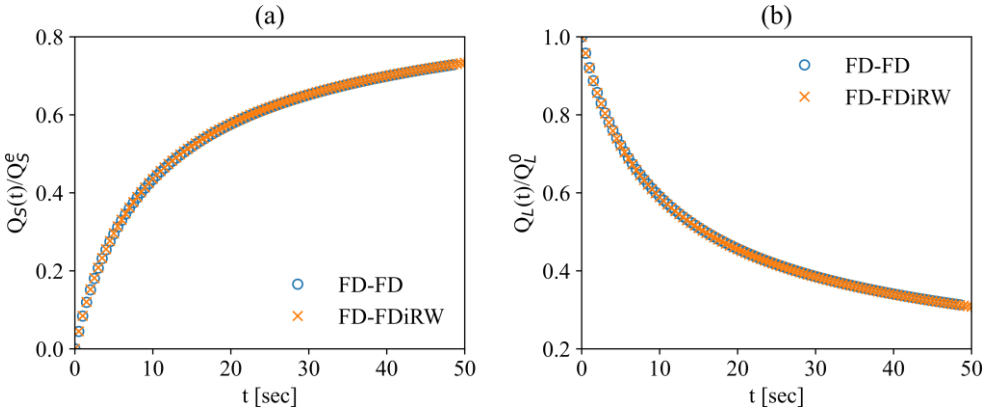

Figure 9 Radionuclide absorption kinetics obtained from simulations. $Q_S(t)$ and $Q_L(t)$ are the instant total concentration of radionuclides in solid and liquid, respectively.

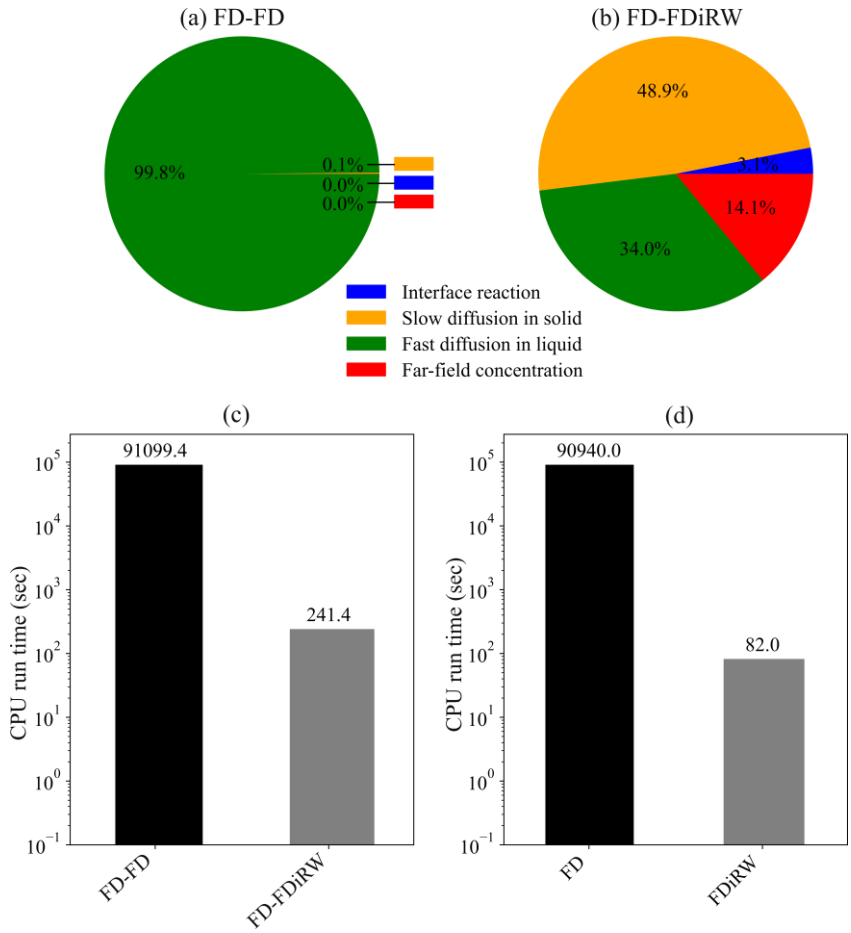

Figure 10 Comparison of CPU run times of FD-FD and FD-FDiRW frameworks for solving the strongly inhomogeneous diffusion problem within the physical time $t = 0.5\ sec$. (a) Computation time proportions of FD-FD; (b) computation time proportions of FD-FDiRW; (c) total CPU run times of FD-FD vs FD-FDiRW; (d) CPU run times spent on fast diffusion part by FD vs FDiRW.

With the verified FDiRW solver, we are now capable of exploring how wasteform particles' thermodynamic and kinetic properties and geometry features, such as particle size and porosity, influence radionuclide absorption kinetics. We applied the FDiRW solver to three different sizes of particles, as depicted in Figure 11, and the numerical results are presented in Figure 12.

The results reveal that larger particles exhibit a more prominent concentration gradient inside the solid particles. In the early stage, the outer surface of particles maintains a higher concentration, while the core area retains a lower concentration, as seen in Figure 12 (a1), (b1), and (c1). This phenomenon is more evident in larger particles. Moreover, regions with larger solid volumes, such as the upper left area in Figure 12 (c1) and (c2), exhibit lower concentrations due to the extended diffusion time required for radionuclide ions to reach those areas. Generally, larger particles with their larger solid volumes

take longer to reach absorption capacity, resulting in slower kinetics compared to smaller particles. This trend is illustrated in Figure 13, where the normalized concentration in large particles converges to 1.0 at a slower rate than in small particles.

The scalability of the proposed FDiRW solver when applied to larger particles or multiple-particle systems is investigated in Figure 14. The computation process of the coarse mesh-based FDiRW solver involves three steps: mapping of concentration from fine mesh to coarse mesh (represented by Eq. (20)), matrix-vector multiplication of the FDiRW algorithm (represented by Eq. (15)), and re-mapping of concentration from coarse mesh to fine mesh (represented by Eq. (21)). Floating-point operations (FLOPs) analysis can be conducted to evaluate the computational complexity or scalability of numerical algorithms. In the FLOPs analysis, we focus on multiplication operations, given their significantly heavier computational burden compared to addition. In the mapping step, the number of FLOPs is apparently dominated by the N_L multiplications, i.e., N_L FLOPs. Relatively, the re-mapping step only needs to assign values of N_l liquid nodes, which requires minor computational resources compared to the multiplication operations in the mapping process. The number of FLOPs required for matrix-vector multiplication in Eq. (15) is $N_{rl} \times N_{rl} + N_{rl}$, including $N_{rl} \times N_{rl}$ FLOPs for computing $\mathbf{P}|_{N_{rl} \times N_{rl}} \mathbf{C}|_{N_{rl} \times 1}$, and N_{rl} FLOPs for computing $P_{BC}|_{N_{rl} \times 1} c_{far-field}$. Hence, the total FLOPs for the coarse mesh-based FDiRW solver are $N_{rl}(N_{rl} + 1) + N_L$. Considering N_L is two orders of magnitude larger than N_{rl} as listed in Table 2, when N_{rl} reaches a level of 10^3 or higher, the computational complexity of FDiRW would be dominated by the matrix-vector multiplication step, i.e., $O(N_{rl}^2)$, based on FLOPs analysis. However, numerical experiments reveal that FDiRW's computational complexity of $O(N_L)$, as shown in Figure 14, is dominated by the mapping and remapping processes, even when N_{rl} goes to as high as 6,000. The discrepancy may be attributed to the frequent access to the index memory of representative nodes corresponding to each node in near-field liquid during the mapping and remapping processes, which potentially causes memory-dominant complexity.

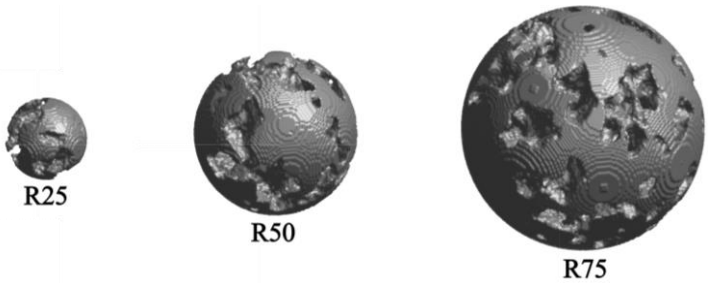

Figure 11 Geometries of three different sizes of porous wasteform particles obtained from phase field modeling. The three particles denoted as R25, R50, R75 have a radius of $25\Delta h, 50\Delta h, 75\Delta h$, respectively.

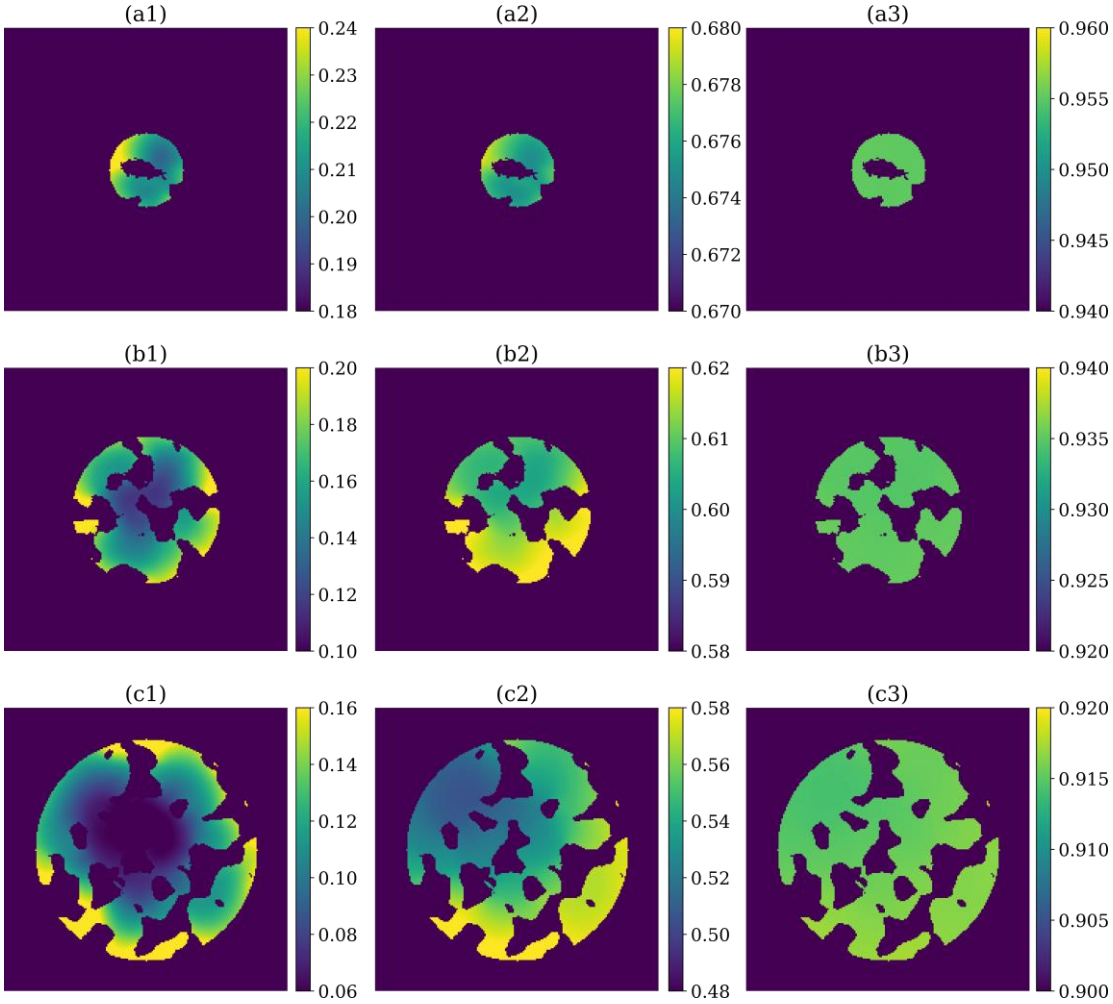

Figure 12 Screenshots of concentration fields obtained from FD-FDiRW at $t = 2$ seconds (a1, b1, c1), $t = 20$ seconds (a2, b2, c2), $t = 200$ seconds (a3, b3, c3) of the three different sizes of particles. Note that, the subplots have different colorbar ranges. Note that, the colorbar range is selected to reflect the gradient of concentration distribution in the solid phase, and the concentration in liquid phase is close to zero.

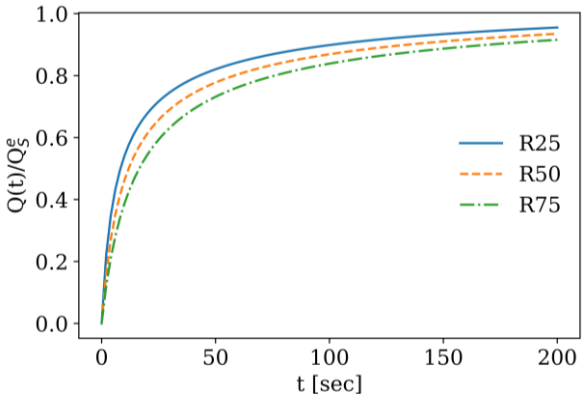

Figure 13 Radionuclide absorption kinetics of different sizes of particles obtained from FD-FDiRW.

Table 2 Total number of nodes and representative nodes in near-field liquid of the three particles R25, R50, R75, and the corresponding CPU running hours in FDiRW computation.

	R25 particle	**R50 particle**	**R75 particle**
$\boldsymbol{N_L}$	67,207	329,404	905,426
$\boldsymbol{N_{rl}}$	561	2,515	6,168
CPU run times [hours]	4.95	9.85	19.81
$\boldsymbol{N_S}$	45,724	366,713	1,238,185
$\boldsymbol{V_L^{far-field}}$	2.27×10^{-11} [mL]	1.80×10^{-10} [mL]	6.16×10^{-10} [mL]

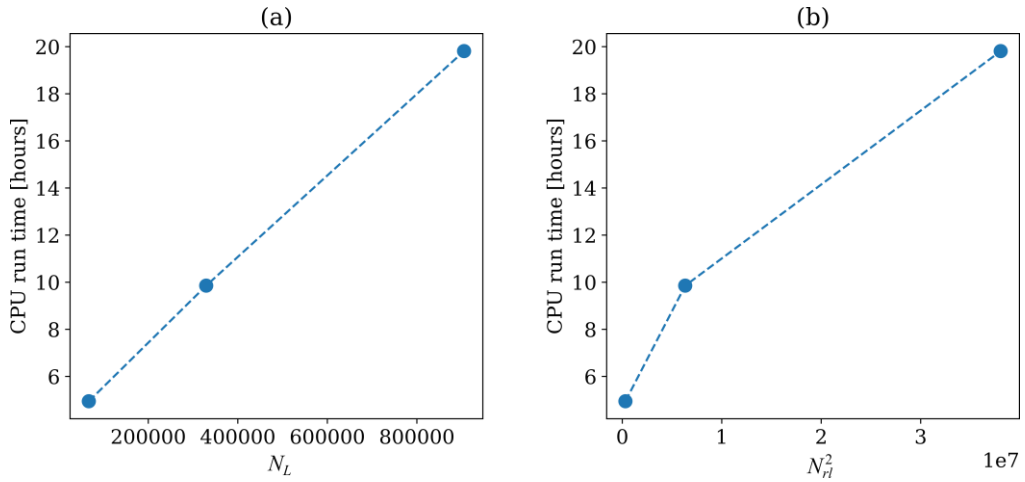

Figure 14 Scalability of FDiRW solver when applied to large size of porous wasteform particles. (a) CPU hours *vs* N_L; (b) CPU hours *vs* N_{rl}. CPU hours is linearly proportional to N_L, meaning the computational complexity of FDiRW is of O(N_L).

5. Conclusions and Discusions

In conclusion, this study introduced and validated an alternative numerical approach, FDiRW, designed to address the computationally intensive fast diffusion process alongside other slower processes in nuclear waste treatment applications with porous wasteform materials. The proposed FDiRW solver demonstrates desirable accuracy, reproducing concentration distributions around the porous wasteform particle and kinetic curves of radionuclide ion absorption similar to the benchmark Finite Difference solutions. It achieves a remarkable efficiency improvement, boasting a 1000x enhancement over the FD method for a medium-sized model of 192×192×192 grids, thanks to its utilization of larger time steps and coarse mesh. Regarding scalability, the computational complexity of the solver is O(N_L) for small model sizes based on numerical tests, but theoretically converges to $O(N_{rl}^2)$ as the model size increases, where N_L and N_{rl} represent the total number of liquid nodes in the fine mesh and coarse mesh, respectively. Thus, the FDiRW approach provides an effective and cost-efficient computational tool for addressing strongly inhomogeneous problems in nature and engineering applications.

For general purpose, this study calculates the concentration at every representative liquid node, forming a square matrix **P**. However, for better efficiency, we find that only representative nodes corresponding to interface liquid nodes are needed for the interface reaction computation in this particular problem. This means that we can reduce the row dimension of **P**, $\mathbf{P}_{BC}$ and **C**, which corresponds to the number of representative nodes connected to the interface, to a smaller level. By doing so, we can significantly reduce the computational demands in the matrix-vector multiplication step, as well as mapping and remapping processes. Therefore, the efficiency of FDiRW solver can be further enhanced by identifying those representative liquid nodes corresponding to interface liquid nodes.

Actually, the application of this FDiRW solver can be extended beyond diffusion equation to include dynamical flow which is a factor accelerating the transport of mobile species in liquid. While our focus in this study is on solving the diffusion equation using the explicit Finite Difference method, the FDiRW approach can effectively tackle diffusion-convection problems by solving the diffusion-convection equation when determining the elements of the coefficient matrix **P**. This extension is feasible as long as the dynamical flow can be regarded as a "pseudo-isolated" process, characterized by a steady state and independence from other processes. Importantly, once the coefficient matrix **P** is determined, the integration of dynamical flow does not affect the matrix-vector multiplication formulation in Eq. (15) neither the mapping/remapping steps. Therefore, incorporating dynamical flow is rather straightforward, and importantly, it does not increase the computational demands of the integrated numerical framework.

Albeit the considerable advantages in computational efficiency and applicability, it is essential to acknowledge a main limitation of the proposed FDiRW approach. This limitation arises from the constraint of fixed fluid domain where the fast diffusion occurs. In other word, FDiRW would fail if the porous structure evolves, causing a changing liquid node set, during the process. In such cases, the coefficient matrix **P** must be updated periodically. However, frequent updates of the **P** matrix can negate the efficiency gains of FDiRW and cause a very complicated implementation procedure by performing multiple iterations of computation to solve the diffusion equation with the explicit Finite Difference method. Nevertheless, the FDiRW has a wide range of applications in nature, featuring strongly inhomogeneous diffusion processes with fixed or slowly evolving microstructures.

Since the FDiRW approach utilizes an explicit time-stepping scheme, where the concentration at the next time-step depends solely on that at the last time-step, both the mapping/remapping step and the matrix-vector multiplication can be executed independently and in parallel. Consequently, FDiRW is well-suited for high-performance parallel computation, particularly the GPU multi-thread parallel computation. Moreover, there's potential for efficiency gains by employing low-precision computation [25] in FDiRW, as the superposition operation of long-time diffusion results does not necessitate high-precision computation as long as concentration conservation is upheld. Therefore, we plan to explore this avenue in our future work.

CRediT authorship contribution statement

Zirui Mao: Investigation, Methodology, Visualization, Writing - original draft. **Yulan Li**: Methodology of phase field model, Discussion, Writing – review & editing. **Robert Montgomery**: Project administration, Writing – review & editing. **Agnes**

Grandjean: Writing – review & editing. **Hans-Conrad zur Loye**: Writing – review & editing. **Shenyang Hu**: Conceptualization, Supervision, Writing - review & editing.

Acknowledgements

The work described in this article was performed by Pacific Northwest National Laboratory, which is operated by Battelle for the U.S. Department of Energy under Contract DE-AC05-76RL01830. This work was supported as part of the Center for Hierarchical Waste Form Materials, an Energy Frontier Research Center funded by the U.S. Department of Energy, Office of Science, Basic Energy Sciences under Award No. DE-SC0016574.

References

1. Eugene Isaacson, H.B.K., *Analysis of Numerical Methods*. 1994: Courier Corporation. 541.
2. G.R. Liu, S.S.Q., *The finite element method: a practical course*. 2013: Butterworth–Heinemann.
3. O.C. Zienkiewicz, R.L.T., J.Z. Zhu, *The finite element method: its basis and fundamentals*. 2005: Elsevier.
4. Mao, Z., G.R. Liu, and M.J. Demkowicz, *An Efficient Finite Difference-based Implicit Solver for Phase-Field Equations with Spatially and Temporally Varying Parameters.* International Journal of Computational Methods, 2024: p. Submitted.
5. Biner, S.B., *Programming Phase-Field Modeling*. 2017: Springer Cham. 400.
6. Liu, G.R. and Z. Mao, *Gradient Smoothing Methods with Programming: Applications to Fluids and Landslides*. 2024: World Scientific Inc.
7. Provatas, N., N. Goldenfeld, and J. Dantzig, *Efficient Computation of Dendritic Microstructures Using Adaptive Mesh Refinement.* Physical Review Letters, 1998-04-13. **80**(15).
8. Folch, R. and M. Plapp, *Quantitative phase-field modeling of two-phase growth.* Physical Review E, 2005-07-07. **72**(1).
9. Zhang, Y., *Simulation of the diffusion process in composite porous media by random walks.* Progress in Natural Science-Materials International, 2005. **15**(12): p. 1117-1125.
10. Qiu, J. and Y.B. Yi, *Random Walk Simulation Model of Diffusion in Circular and Elliptical Particulate Composites.* International Journal for Multiscale Computational Engineering, 2018. **16**(2): p. 131-142.
11. Alemany, I., et al., *Random walk diffusion simulations in semi-permeable layered media with varying diffusivity.* Scientific Reports, 2022. **12**(1).
12. Plapp, M. and A. Karma, *Multiscale Random-Walk Algorithm for Simulating Interfacial Pattern Formation.* Physical Review Letters, 2000-02-21. **84**(8).
13. Enke, D., R. Gläser, and U. Tallarek, *Sol-Gel and Porous Glass-Based Silica Monoliths with Hierarchical Pore Structure for Solid-Liquid Catalysis.* Chemie Ingenieur Technik, 2016/11/01. **88**(11).
14. Merceille, A., et al., *Effect of the synthesis temperature of sodium nonatitanate on batch kinetics of strontium-ion adsorption from aqueous solution.* Adsorption 2011 17:6, 2011-09-23. **17**(6).
15. Bilel Said, et al., *LTA zeolite monoliths with hierarchical trimodal porosity as highly efficient microreactors for strontium capture in continuous flow.* Microporous and Mesoporous Materials, 2016/09/15. **232**.
16. Vanýsek, P., *Ionic conductivity and diffusion at infinite dilution*, in *Handbook of Chemistry and Physics*. 1992, CRC Press: Boca Raton. p. 111-113.
17. Gaus, H. and W. Lutze, *Kinetics of Sr/Ba and Sr/Ca Ion Exchange in Synthetic Zeolite A.* J. Physc. Chem., 1981. **85**: p. 79-84.
18. Zirui Mao, X.Z., Yulan Li, Vanessa Proust, Alban Gossard, Thomas David, Robert Montgomery, Agnes Grandjean, Huidan Yu, Hans-Conrad zur Loye, Shenyang Hu, *Phase field-volumetric lattice Boltzmann model of ion uptake in porous nuclear waste form materials under continuous flow.* Journal of Nuclear Materials, 2024. **596**: p. 155103.

19. Mao, Z., et al., *Simulations of Ionic Exchange Kinetics for the Cs Removal in Porous Particles.* Journal of Nuclear Materials, 2024: p. In submission.
20. Yulan Li, S.H., Robert Montgomery, Agnes Grandjean, Theodore Besmann, Hans-Conrad zur Loye, *Effect of charge and anisotropic diffusivity on ion exchange kinetics in nuclear waste form materials.* Journal of Nuclear Materials, 2022. **572**: p. 154077.
21. Proust, V., et al., *Design and characterization of hierarchical aluminosilicate composite materials for Cs entrapment: Adsorption efficiency tied to microstructure.* Journal of Water Process Engineering, 2023. **51**: p. 103381.
22. Mao, Z., et al., *A Finite Difference informed Random Walk solver for simulating radiation defect evolution in polycrystalline structures with strongly inhomogeneous diffusivity.* Computational Materials Science, 2025/01/01. **246**.
23. Hu, S., Z. Mao, and B. Peeler, *An integrated mesoscale model of creep in polycrystalline UMo fuels under irradiation.* NPJ computational materials, 2024: p. in submission.
24. Carslaw, H.S. and J.C. Jaeger, *Conduction of heat in solids (2nd ed.)*. 1959, Oxford: Oxford University Press.
25. Zirui Mao, X.L., Shenyang Hu, Ganesh Gopalakrishnan, Ang Li, *A GPU accelerated mixed-precision Smoothed Particle Hydrodynamics framework with cell-based relative coordinates.* Engineering Analysis with Boundary Elements, 2024. **161**: p. 113-125.